Hydrodynamic interactions change the buckling threshold of parallel flexible sheets in shear flow

Hugo Perrin ●,* Heng Li ●,* and Lorenzo Botto†
Process & Energy Department, Faculty of Mechanical, Maritime and Materials Engineering,
Delft University of Technology, Delft, The Netherlands

Buckling induced by viscous flow changes the shape of sheetlike nanomaterial particles suspended in liquids. This instability at the particle scale affects collective behavior of suspension flows and has many technological and biological implications. Here, we investigated the effect of viscous hydrodynamic interactions on the morphology of flexible sheets. By analyzing a model experiment using thin sheets suspended in a shear cell, we found that a pair of sheets can bend for a shear rate ten times lower than the buckling threshold defined for a single sheet. This effect is caused by a lateral hydrodynamic force that arises from the disturbance flow field induced by the neighboring sheet. The lateral hydrodynamic force removes the buckling instability but massively enhances the bending deformation. For small separations between sheets, lubrication forces prevail and prevent deformation. Those two opposing effects result in a nonmonotonic relation between distances and shear rate for bending. Our study suggests that the morphology of sheetlike particles in suspensions is not purely a material property but also depends on particle concentration and microstructure.

I. INTRODUCTION

Soft biological or synthetic objects, such as cells, lipid bilayers, macromolecules, and nanoparticles, can deform when suspended in sufficiently strong shear or extensional flows [1–4]. Predicting flow-induced morphological changes is crucial in many fields, ranging from biophysics, where swimming of micro-organisms relies on fluid-structure interactions [5], to soft matter physics, where the rheological response of a particulate suspension is affected by the instantaneous particle shape [6]. Model studies in canonical flows have provided profound physical insights of general applicability. For example, the theoretical prediction of the coil-stretch transition of polymers in simple shear flow [7,8] was instrumental in the development of rheological models for dilute polymer solutions [9].

The recent need to develop liquid-based methods to process two-dimensional (2D) nanomaterials [10–12] has triggered new interest on the effect of flow on the morphology of sheetlike materials [3,10,11,13–17]. Two-dimensional materials have low bending modulii and therefore can undergo transient or permanent buckling in flow [3]. Recent numerical studies [3,18] demonstrate that purely mechanical models based on the competition between hydrodynamic compressive force and elastic-bending forces can capture the change of morphology of isolated graphene sheet and 2D polymers suspended in a simple shear flow. This agreement demonstrates that the morphology of a single sheet is determined by a buckling instability whose threshold depends, for a given fluid shear rate and viscosity, only on the bending modulus and length of the sheet. However, the extension of

---

*These authors contributed equally to this work.
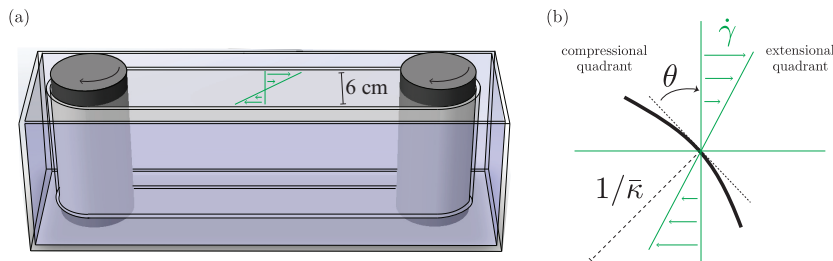†Corresponding author: l.botto@tudelft.nl

FIG. 1. (a) Schematic of the shear cell. (b) Schematic of a buckled sheet viewed along the vorticity direction of the shear flow and definition of the midpoint orientation angle θ and midpoint curvature $\bar{\kappa}$. The compressional quadrant and the extensional quadrant are shown. In this schematic, the sheet is oriented in the compressional quadrant ($-\pi/2 < \theta < 0$).

this result to suspensions of many particles is an open question. Because of their relatively large contact area, sheetlike particles are prone to stacking at small interparticle separations [11,19]. Hydrodynamic interactions between nearly parallel sheets are thus expected to alter the buckling dynamics predicted for single sheets.

In this study we investigate parallel pairs of flexible sheets in a shear flow as a function of their separation distance, and study how the buckling instability threshold depends on hydrodynamic interactions. By performing model experiments, and interpreting the results with the help of boundary-integral simulations and theoretical modeling, we demonstrate that hydrodynamic interactions can trigger bending far below the buckling threshold of a single sheet. Hydrodynamic interactions cannot therefore be considered second-order effects when predicting the morphology of flexible sheets in flow. More specifically, our simulations and theoretical modeling show that the dipolar disturbance flow field induced by each sheet gives rise to a lateral hydrodynamic force. This lateral force modifies the mechanical response of the sheet pair to the compressive axial hydrodynamic force experienced when the pair is oriented in the compressional quadrant of the shear flow. However, for small separations, the lubrication forces overcome this dipolar contribution and prevent bending. These two competing effects result in a nonmonotonic relation between interparticle distance and critical shear rate for buckling. More generally, our results suggest that the deformation of close sheets in a suspension may not only depend on the mechanical and geometric properties of each sheet but also strongly on the pair-particle separation and thus on the concentration.

II. EXPERIMENTS

Mylar sheets (Young's modulus $E \simeq 4$ GPa) of different thicknesses ($h = 23, \ 50, \ \text{and} \ 125 \ \mu\text{m}$), width $w = 1$ cm, and length L ranging from 1 to 4 cm were used. Corresponding sheet bending modulii are $B \simeq 5.0 \times 10^{-6}, \ 5.0 \times 10^{-5}, \ \text{and} \ 8.1 \times 10^{-4}$ J [$B = Eh^3/12(1 - \nu^2)$ where $\nu \simeq 0.5$ is the Poisson's ratio]. The shear cell is composed of a belt driven by two corotating cylinders of diameter 6 cm—see Fig. 1(a). A motor, connected to one of the cylinders, imposes a controlled shear rate in the range $\dot{\gamma} = 0.4 - 10 \ \text{s}^{-1}$. The design of the shear cell is essentially identical to the one described in Ref. [20], so we refer to that publication for construction details. The flow cell allows to generate a flow that, in the central region away from the cylinders, is essentially a two-dimensional simple shear flow (the flow profile was measured by particle image velocimetry [21]). We considered single sheets, and pairs of parallel sheets with separation distance d varying in the range $d/L = 0.03-1$. The sheets were placed in glycerol (the viscosity is $\eta \simeq 1$ Pa s and the density is $\rho \simeq 1.2 \times 10^3 \ \text{kg m}^{-3}$). Mylar is slightly more dense than glycerol, and the difference between their densities is $\Delta\rho \simeq 10^2 \text{kg m}^{-3}$. The sedimentation time over one sheet length is of the order of 10^3s, which is about $100\dot{\gamma}^{-1}$ for the lowest shear rate. Furthermore, the sedimentation is in the vorticity direction so the motion of the sheet along the vertical direction does not

affect the essentially two-dimensional dynamics of the sheets. The maximum Reynolds number $\mathrm{Re} = \rho \dot{\gamma} L^2 / \eta$ is of order 1 at the maximum shear rate. The sheets were immersed in the liquid when the belts were not in motion (zero flow velocity), and manipulated with tweezers so that their normal was in the plane of the flow. When studying sheet pairs, the sheets were placed parallel to each other and the separation distance d measured. After placing the sheets, the motor driving the belts was switched on. Data from experiments in which the sheets were not sufficiently parallel were discarded. The criterion for parallelism was that the initial angle between the two sheets must not be greater than $2°$. During the dynamics, the normal vector remains in the flow-gradient plane and thus the dynamics is two-dimensional. Optical measurements with a camera were carried out from the top, i.e., along the vorticity direction of the undisturbed shear flow, with a time resolution of 0.1 s and with a spatial resolution of 25 μm/pixel. Sheet profile detection is performed manually using imageJ software. We extracted the midpoint orientation angle $\theta(t)$ by fitting a line to each sheet's profile—see Fig. 1(b). The midpoint curvature $\bar{\kappa}(t)$ was obtained by fitting a parabola to each sheet's profile. We detected and analyzed sheet profiles at maximum temporal resolution only when there was a significant temporal variation in angle or curvature. For this reason, the temporal density of data points seen in the graphs is not uniform. As explained in Sec. II of the Supplemental Material [21], for the few (about 1 in 100) images that were not captured due to a camera software problem, we used linear interpolation to account for the small temporal gap between images. Even though the maximum Re is of order 1, in analyzing the results we will consider a low Reynolds approximation (Stokes flow). As it will appear later, this approximation gives a reasonable agreement between the simulations and the experimental data.

III. SIMULATION METHOD

We simulated the fluid-structure interaction of thin sheets in Stokes flow by a regularized Stokeslet approach [17,22–24]. The regularized Stokeslet method has been used to study a variety of fluid-structure interaction problems at low Reynolds number, including cilia-driven transport [22], flagella synchronization [23], and flow around double helices [24]. As in the experiment the flow and the sheet dynamics are two-dimensional, we simplified the simulation choosing a two-dimensional description. For a two-dimensional slender body, the approach consists in placing regularized force singularities along the body's centerline. The integral of the regularized force density over each discretization line segment represents the force exerted by that segment of the slender body on the fluid. Owing to the linearity of the Stokes equation, the velocity field $\mathbf{u}(\mathbf{x}, t)$ at position $\mathbf{x}$ and time t obeys the following boundary integral equation [25]:

$$\mathbf{u}(\mathbf{x}, t) = \mathbf{u}^\infty(\mathbf{x}) + \frac{1}{4\pi\eta} \int_C \mathbf{G}_\epsilon(\mathbf{x}, \mathbf{x}_0) \cdot \mathbf{f}(\mathbf{x}_0, t) dl, \tag{1}$$

where $\mathbf{u}^\infty$ is the undisturbed background flow, η is the dynamic viscosity, $\mathbf{f}(\mathbf{x}_0, t)$ is the force density exerted on the fluid by the sheet element dl centered at $\mathbf{x}_0$ and $\mathbf{G}_\epsilon$ is a 2D regularized Stokeslet for an unbounded flow [26]. Here, we neglected the double-layer potential because of the inextensibility approximation for the sheets [17,24]. Since the sheets are inertia-less, the hydrodynamic force $(-\mathbf{f})$ is balanced by the local internal elastic force. Numerically, we compute the elastic force from the derivative of the bending energy, as done in Refs. [17,23,27]. A very large value of the spring stretching constant was used to model the inextensibility of the sheets. The maximum relative elongation of the sheet during the dynamics was typically not larger than 10^{-3}. The kinematics of each sheet is governed by the no-slip boundary condition on the surface of the sheet. In the slender body approximation, this condition is approximated by a no-slip condition at the centerline of the sheet:

$$\frac{\partial \mathbf{X}(s, t)}{\partial t} = \mathbf{u}(\mathbf{X}(s, t)), \tag{2}$$

where $\mathbf{X}(s, t)$ is the position vector along the centerline of the sheet at the curvilinear coordinate s and time t. In this numerical method the sheet has zero thickness, therefore to observe tumbling and bending, the sheet needs to be initialized at an orientation angle different from $\pm \pi/2$ and the initial shape set to a perturbation from a straight line [28]. Based on our previous work [17] we chose for the initial orientation $\theta_0 = -\pi/2 + \pi/10$ and for the initial shape perturbation the first buckling mode $\kappa(s) = \kappa_0 \sin(s\pi/L)$ with a small amplitude $\kappa_0 = 8 \times 10^{-3}/L$, where $\kappa(s)$ is the local curvature at s. At each time step, the velocity field is calculated first by Eq. (1), then Eq. (2) is advanced in time by a first-order explicit Euler scheme to obtain the sheet's configuration at the new time step. In the simulations, each sheet is discretized by 51 nodes and the time step is $10^{-5}\dot{\gamma}^{-1}$. Validations of the code on two cases for which asymptotic solutions are known can be found in our previous article [17]. Those two cases are the relaxation of an initially deformed sheet in a quiescent flow and the tumbling dynamics of a single sheet in a shear flow. During the simulation, at each time step the midpoint curvature $\bar{\kappa}(t) = \kappa(s = L/2, t)$ of a sheet is calculated by fitting a parabola to its center.

IV. DYNAMICS OF A SINGLE SHEET

For an inextensible flexible sheet of length L, width w, and bending modulus B, the Euler buckling force for axial compression scales proportionally to wB/L^2 [29,30]. The viscous compressive force in a shear flow in the Stokes limit scales as $\eta \dot{\gamma} L w$. Its dependence on the orientation angle is $-2 \sin\theta \cos\theta$ [3,31], which is maximum when the sheet is oriented along the compressional axis $\theta = -\pi/4$ of the shear flow [see Fig. 1(b)]. The buckling dynamics of a single flexible sheet depends therefore on the elastoviscous number [3]

$$E_v = \frac{\eta \dot{\gamma} L^3}{B}. \tag{3}$$

This nondimensional number can be also interpreted as the ratio of two timescales: $1/\dot{\gamma}$, the characteristic timescale of the shear flow, and $\eta L^3/B$, the characteristic timescale of curvature relaxation in a quiescent viscous liquid.

We determined the single-sheet buckling threshold by measuring experimentally the sheet curvature $\bar{\kappa}$ corresponding to different elastoviscous numbers, placing only one sheet in the shear cell. The Mylar sheet is practically perfectly flat when not subject to external forces. The residual curvature of each sheet, if at all present, is at most $0.02/L$. For small elastoviscous numbers, the sheet tumbles in the flow and remains straight. For relatively large elastoviscous numbers, for example $E_v \simeq 21$ [Fig. 2(a)], the sheet deforms during tumbling. The time dependence of the angle $\theta(t)$ in Fig. 2(a) is well described by Jeffery's solution for rigid oblate ellipsoids [3,32,33]. This agreement validates the Stokes flow assumption we made for the simulations. This agreement also shows that the tumbling dynamics is not significantly affected by the sheets deformations for curvatures smaller than $1/L$. The time-dependent curvature is seen to grow when the sheet is oriented in the compressional quadrant $(-\pi/2 < \theta < 0)$, which is the signature of the buckling instability. Then the curvature decays to zero, over a timescale $1/\dot{\gamma}$. It is interesting to note that the curvature decays also in the compressional quadrant, likely because for $(-\pi/4 < \theta < 0)$, the hydrodynamic forces are predominantly compressive but their magnitude is below the threshold for buckling. As $\theta(t)$ spans the extensional quadrant $(0 < \theta < \pi/2)$, the curvature decays monotonically to zero. To identify the single-sheet buckling threshold, we measured the maximum curvature $\bar{\kappa}_{\max}$ attained during a tumbling cycle for different elastoviscous numbers [see Fig. 2(b)]. The results lie in two regions separated by a critical elastoviscous number $E_v^c \simeq 11 \pm 3$ above which the sheet always deforms with a curvature larger than the experimental resolution. The maximum curvature measured in experiments seems to increase proportionally to E_v^2 [21]. Below this number the sheets curvature is negligible. We defined the critical value of E_v as the threshold value above which sheets always deform. The uncertainty in the determination of E_v^c was estimated from the dispersion of the data points [21]. To corroborate this observation, we performed numerical simulations of single
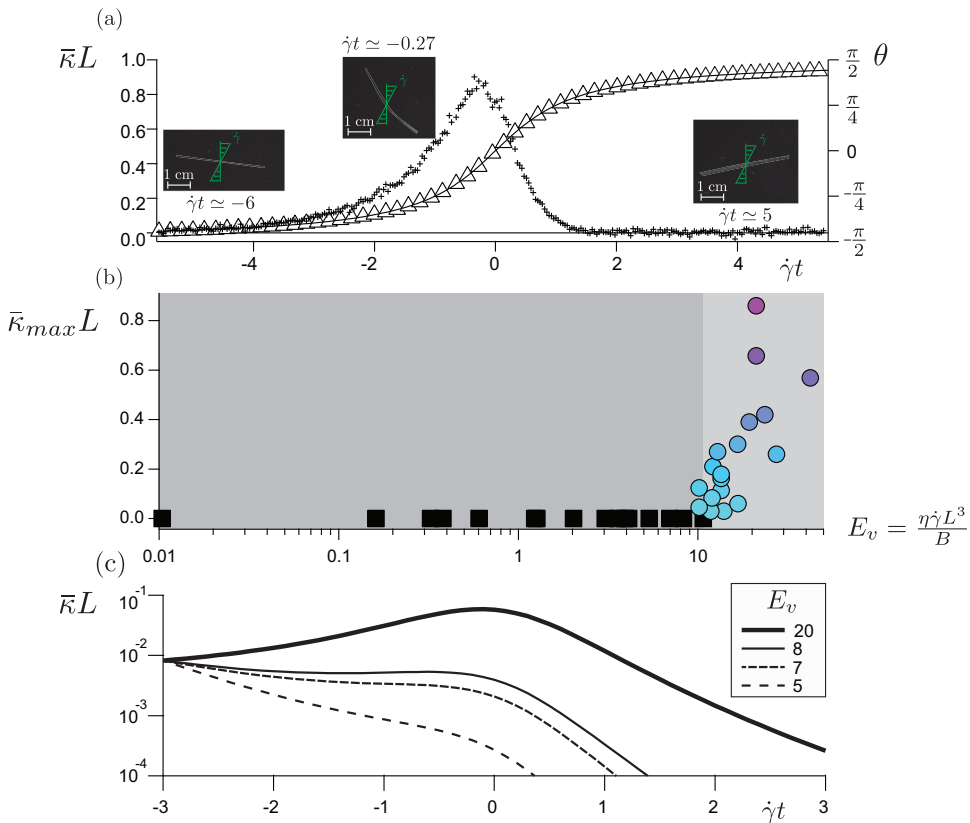
FIG. 2. (a) Normalized midpoint curvature $\bar{\kappa}L$ (crosses) and midpoint orientation angle θ (triangular markers) versus rescaled time $\dot{\gamma}t$ for $E_v \simeq 21$. Time has been shifted so that $\dot{\gamma}t = 0$ corresponds to the orientation $\theta = 0$. The black line is Jeffery's prediction $\theta(t) = \arctan(\dot{\gamma}t)$ [32]. (b) Maximum normalized curvature versus elastoviscous number for a single sheet. The dark and light grey regions delimit the rigid limit and the buckling region, respectively. The measured critical elastoviscous number from this diagram is $E_v^c \simeq 11$. (c) Normalized curvature versus normalized time from dynamic simulations of a single sheet for different elastoviscous numbers.

sheets for different elastoviscous numbers, see Fig. 2(c). For elastoviscous numbers larger than $E_v = 8$, the curvature increases in time, signature of the growth of the buckling instability. For elastoviscous numbers smaller than $E_v = 8$, the curvature decays. The simulations confirm that the maximum curvature increases approximately as $\sim E_v^2$ for relatively small values of E_v [21]. The agreement between the numerical prediction ($\simeq 8$) and the experimental value ($\simeq 11$) is acceptable considering the finite experimental resolution, which makes a very precise determination of the buckling threshold difficult [31]. A mathematical model for the buckling of a thin flexible circular disk, based on applying Jeffery's solution for the hydrodynamic stress on an oblate ellipsoids to predict the compressive load on the disk, predicted a threshold values $\simeq 10^2$ [34]. Recent simulations of an hexagonal flexible sheet modeled as a collection of beads interacting via long-range hydrodynamic interactions—represented at the Rotne-Prager-Yamakawa level—suggested a critical buckling threshold in simple shear flow of about 50 [3]. Since both the hydrodynamic compressive force and the elastic response of the sheet depend on the shape, it is expected that the buckling threshold for rectangular sheets is different than the ones for circular disks or hexagonal sheets, so differences with published work are expected. The experimental determination of the buckling
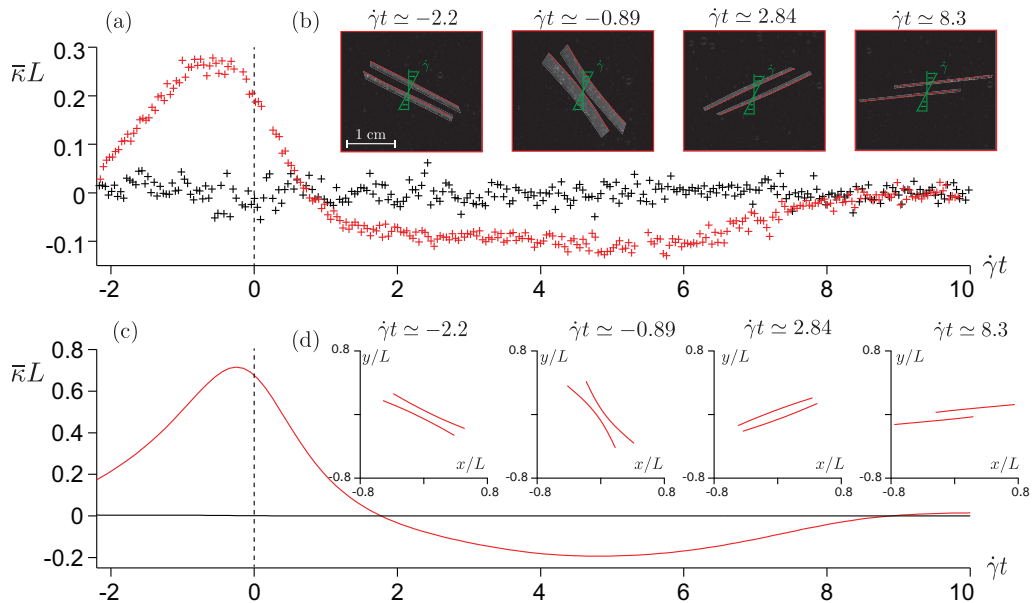
FIG. 3. Comparison between single sheet dynamics and dynamics of a pair of parallel sheets below the single-sheet buckling threshold. (a) Experimental normalized curvature $\bar{\kappa}L$ versus normalized time $\dot{\gamma}t$ for a single sheet (in black) and a sheet pair separated by $d/L \simeq 0.2$ (in red) for $E_v \simeq 3.6$. (b) Images of a pair of parallel sheets at two selected times. (c) Normalized curvature $\bar{\kappa}L$ versus normalized time $\dot{\gamma}t$ for simulation of a single sheet (in black) and a pair of sheets separated by $d/L = 0.1$ (in red) for $E_v = 7$. (d) Simulated shapes of a pair of parallel sheets corresponding to the two selected times of panel (b).

threshold for single rectangular sheets, confirmed by our numerical simulation, is an important step that provides a reference case for the study of pairs of parallel sheets.

V. DYNAMICS OF A PAIR OF PARALLEL SHEETS

A body formed by two sheets bonded together by adhesion or friction has a larger bending rigidity than a single sheet [30,35,36]. Therefore, one may intuitively assume that two sheets separated by a layer of viscous liquid would have a larger buckling threshold than a single sheet. In contrast, we found that a pair of parallel sheets can deform for values of E_v below the single-sheet threshold. For example, for $E_v \simeq 3.6$ the single-sheet curvature is negligible (see Fig. 2(b) and Fig. 3(a) [37]) while for the same parameter two sheets separated by $d/L \simeq 0.2$ display a finite curvature. The curvature of the two sheets increases with time, then decreases, changes sign and finally decays to zero at the end of the tumbling motion [see Fig. 3(a)]. In the single-sheet case, for $E_v > E_v^c$ the curvature relaxes while the sheet is oriented in the extensional quadrant [see Fig. 2(a)]. In contrast, pair of sheets deform while oriented in the extensional quadrant [Fig. 3(b) right panel]. These two changes of behavior for a pair of sheets, bending below the buckling threshold and bending in the extensional quadrant, are consequences of hydrodynamic interactions between the sheets, as it will be demonstrated below. A further example illustrating how the curvature changes with time for $d/L \simeq 0.04$ and $E_v \simeq 12.8$ is given in the Supplemental Material [21].

To rationalize the experimental observations, we simulated the dynamics of two parallel flexible sheets. For $E_v = 7$, the simulations indicate that the single sheet dynamics is stable: a small initial curvature decreases in time—see the black line in Fig. 3(c). For a pair of parallel sheets separated by a distance $d = 0.1L$ and the same value $E_v = 7$, the computed curvature follows qualitatively
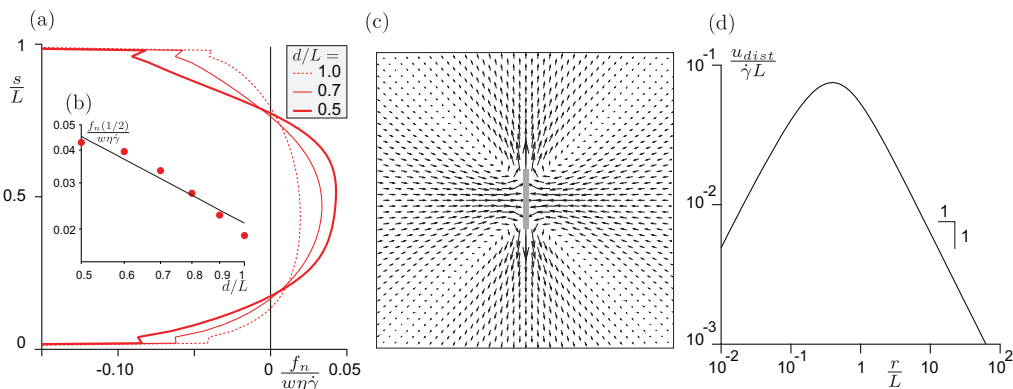
FIG. 4. Hydrodynamic interactions from simulation. (a) Lateral force induced by the first sheet on the second sheet in the case of two parallel sheets in a shear flow, oriented in the compressional quadrant (at $\theta_0 = -\pi/2 + \pi/10$), for $d/L = 1, 0.7,$ and 0.5. (b) Magnitude of the lateral force at the center of the sheet versus the separation distance when the sheets are oriented in the compressional quadrant (at $\theta_0 = -\pi/2 + \pi/10$). The line is the best fit $y = Ax^\alpha$ with $A \simeq 0.02$ and $\alpha \simeq -1.1$. (c) Vector plot of the 2D disturbance flow. The rectangle represents the sheet. (d) Magnitude of the disturbance flow velocity u_{dist} induced by a sheet in a 2D compressional flow, versus the distance r measured orthogonally to the sheet.

the experimental dynamics, see the red line in Fig. 3(c): each sheet of the pair deforms, adopts a concave shape in the compressional quadrant [Fig. 3(d), left panel], then the curvature changes sign, the sheets adopt a convex shape in the extensional quadrant [Fig. 3(d), right panel] and finally the deformation relaxes to zero. Because in the simulation only hydrodynamic interactions are accounted for, the simulation results support the hydrodynamic origin of the two changes of behavior discussed above in relation to experiments.

From the numerical simulations of two sheets we computed the lateral force on one of the two sheets, when oriented in the compressional quadrant and for varying distance d/L; see Fig. 4(a). The lateral force is nonuniform along the sheet, with a maximum value in the center of the sheet and minima located at the two edges. The force distribution can be described, to a first approximation, as a parabola. As d/L increases it is seen from Fig. 4(b) that the amplitude of the parabolic profile decreases, following a power law with an exponent close to -1. To explain and model this lateral force, we quantified the disturbance flow field set up by a sheet. Because the sheet is inertia-less and the flow 2D, the disturbance flow field in the far field is that of a 2D force dipole whose amplitude decreases as $1/r$ [38], where r is the distance from the geometric center of the sheet. The flow disturbance induced by a body oriented along the compressional or extensional axis of a shear flow can be approximated by placing an elongated particle in a two-dimensional purely straining flow [39], with the long axis of the particle along the extensional direction. We performed simulations with this simplified flow configuration. The computed vector plots in Fig. 4(c) illustrate the dipolar characteristics of the flow, where it is seen that the spatial variation of the flow corresponds to the parabolic distribution of the lateral force. The amplitude of the disturbance flow field is reasonably well captured by a $1/r$ dependence for r as small as $0.5L$ [see Fig. 4(d)]. The sign of the background straining flow governs the sign of the dipole: with our convention the sign is positive for compressional background flow and negative for extensional background flow. Hence, the simulations show that the presence of one sheet generates a parabolic lateral force on the other sheet; this lateral force originates from the disturbance dipole flow field, its amplitude scales as L/d and its sign is governed by the background flow field, being positive when the sheets are in the compressional quadrant and negative in the extensional quadrant.

The information above enables to construct a minimalistic model of flow-induced shape changes that takes into account the dependence on sheet-to-sheet distance. From a balance of forces and moments on an inextensible sheet, in the linear approximation the curvature κ obeys the Euler-Bernoulli equation

$$Bw\frac{d^2\kappa}{ds^2} - T_t(s)\kappa(s) - f_n(s) = 0, \tag{4}$$

where s is the curvilinear coordinate, f_n is the lateral hydrodynamic force per unit length, and T_t is the axial tension [30,40]. The axial tension satisfies

$$\frac{dT_t}{ds} + f_t(s) = 0, \tag{5}$$

where f_t is the axial hydrodynamic force per unit length [30,40]. To model f_n and f_t we used a quasistatic approximation that consists of two main assumptions. First, we neglected the effect of the lateral hydrodynamic drag force caused by the time variation of the curvature. Second, we assume that the curvature is only coupled to the orientation θ through the amplitude of f_t, which we assume to be $-2\sin\theta\cos\theta$. Considering the two extreme cases $\theta = -\pi/4$ (orientation at maximum compression) and $\theta = \pi/4$ (orientation at maximum extension) and modeling the axial force per unit length as an edge force arising from the straining component of the imposed shear rate, we obtain $T_t = -\eta\dot{\gamma}Lw$ for $\theta = -\pi/4$ and $T_t = \eta\dot{\gamma}Lw$ for $\theta = \pi/4$. Fitting the results of our numerical simulations, we modeled the lateral force per unit length arising from the dipolar flow field as

$$f_n(s) = \pm w\frac{L}{d}\eta\dot{\gamma}Kg(s), \tag{6}$$

where the sign depends on whether the sheet is oriented along the compressional or the extensional axis. The function $g(s) = \frac{1}{12} - (\frac{s}{L} - \frac{1}{2})^2$ is a symmetric parabola of zero mean that reproduces the spatial variation of the lateral force seen in Fig. 4(a) and K is a numerical prefactor. We estimated $K \simeq 0.4$ from the force amplitude computed at the orientation θ_0, see Fig. 4(b) (by definition $K = A g(1/2)/2\sin\theta_0\cos\theta_0$, where A is a fitting parameter). The moment balance then reads

$$\frac{d^2\tilde{\kappa}}{d\tilde{s}^2} \pm E_v\left(\tilde{\kappa}(\tilde{s}) - \frac{K}{\tilde{d}}g(\tilde{s})\right) = 0, \tag{7}$$

where $\tilde{\kappa} = \kappa L$, $\tilde{s} = s/L$, and $\tilde{d} = d/L$. The "+" sign corresponds to the maximum compression ($\theta = -\pi/4$). The "−" sign corresponds to the maximum extension ($\theta = +\pi/4$). At maximum compression, for the single sheet case ($1/\tilde{d} \to 0$) this differential equation reduces to the classical Euler-buckling equation for an edge axial load. If $E_v = \pi^2$, then the Euler-buckling equation admits two solutions verifying the free end boundary conditions $\tilde{\kappa}(0) = \tilde{\kappa}(1) = 0$. One solution is the trivial solution $\tilde{\kappa}(\tilde{s}) = 0$ and the other is the first buckling mode $\tilde{\kappa}(\tilde{s}) = \tilde{\kappa}_0\sin(\pi\tilde{s})$ for a purely axial load. The value of the buckling threshold, here π^2, corresponds to a uniform axial tension. However, it can be shown that for a more realistic model of the axial hydrodynamic force $f_t(s)$, i.e., a linear variation of $f_t(s)$ along the sheet [31] for which the axial tension is a parabola, the threshold is reduced by only 15% with respect to π^2. Therefore, the model of uniform axial tension captures the essential behavior of buckling. The value $E_v^c = 11 \pm 3$ we measured experimentally is comparable with the prediction π^2 of this minimal model. However, at the maximum compression, for finite $\tilde{d}$ Eq. (7) admits only one solution satisfying the boundary conditions for any given value of E_v:

$$\tilde{\kappa}(\tilde{s}) = \frac{K}{6\tilde{d}E_v}\{[E_v(-6(\tilde{s}-1)\tilde{s} - 1) + 12] + (E_v - 12)\cos(\sqrt{E_v}\tilde{s})$$
$$+ (E_v - 12)\tan(\sqrt{E_v}/2)\sin(\sqrt{E_v}\tilde{s})\}. \tag{8}$$

The existence of a unique nonzero solution means that there is no buckling instability in the strict sense. Hydrodynamic interactions remove the buckling instability and the curvature has a finite
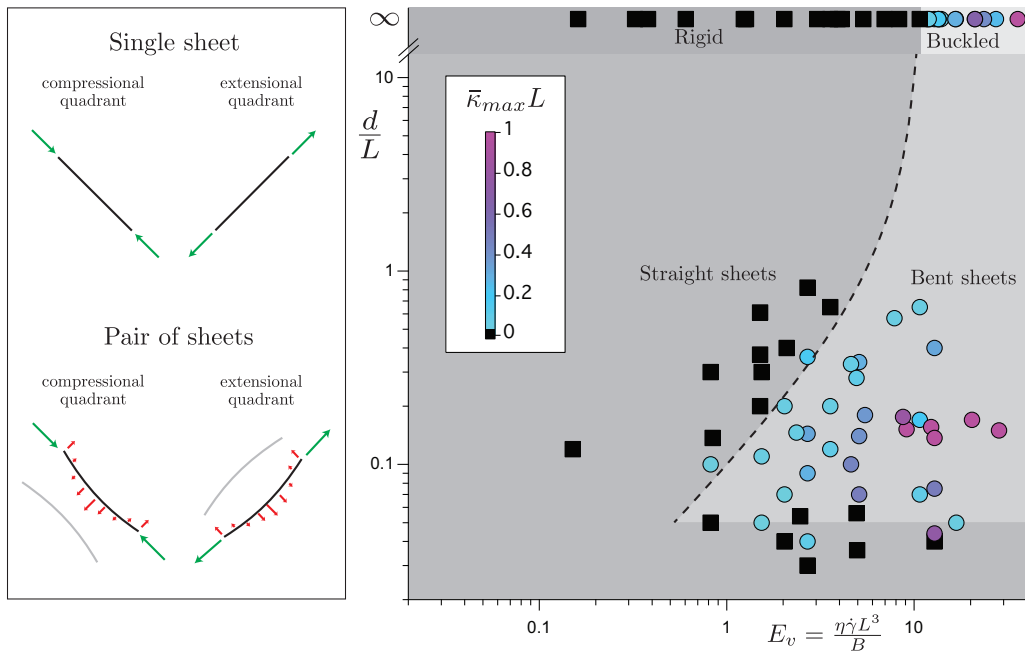
FIG. 5. Left panel: sketch of the hydrodynamic forces distribution in the single and two sheet cases. The black line segments represent the sheets. The green arrows represent the compressional or extensional tangential forces. The red arrows represent the dipolar lateral forces. For $E_v < E_v^c$ the single sheet remains straight while the pair of sheets adopts concave and convex shapes. Right panel: morphology diagram. Maximum normalized curvature for different normalized separation distances d/L and elastoviscous numbers $E_v = \eta\dot{\gamma}L^3/B$. The black squares correspond to deformation below the experimental resolution $\kappa_r = 0.02/L$, the color circles to a finite curvature. The shadow regions are guides for the eye. The experimental data for single sheets of Fig. 2(b) are reported in correspondence to $d/L = \infty$. The equation of the dashed line is $d/L = KE_v/[\kappa_r L(E_v^c - E_v)]$, with $E_v^c = 11$, $\kappa_r L = 0.02$, and $K = 0.02$. The dashed line is plotted for $d/L > 0.05$.

bending amplitude for all values of E_v. To summarize, for a single sheet in pure compression there is a buckling instability while for a pair of sheets, there is no buckling instability but bending deformations do occur. Taking the limits $E_v \to 0$ and $E_v - E_v^c \to 0$ with $E_v < E_v^c$, one can derive from Eq. (8) the following approximation for the maximum curvature (at $\theta = -\pi/4$) of the midpoint of the sheet:

$$\bar{\kappa} \sim +K\frac{L}{d}\frac{E_v}{E_v^c - E_v}. \tag{9}$$

Here we have indicated explicitly the sign of the lateral force, the " $+$ " sign corresponding to the compressional quadrant. In the extensional quadrant, by solving Eq. (7), one can show that the curvature scales as $\bar{\kappa} \sim -KE_v L/d$. As illustrated in the sketch on the left panel of Fig. 5, the change of sign of the dipole force as the sheet tumbles explains the change from concave to convex morphologies seen in Fig. 3(b). Equation (7) is linear, so the scaling in L/d for the dipole amplitude determines the dependence of the bending curvature with respect to d.

To evaluate the ability of the model above to capture essential features of the experimental data, for each value of the parameters $(E_v, d/L)$, we measured the maximum rescaled curvature $\bar{\kappa}_{\max}L$ during tumbling. For pair of sheets, the results indicate two regions of behavior (see right panel Fig. 5). A first region where each sheet's curvature is lower than the experimental resolution. The

label "Straight" in the figure indicates this first region. And a second region where the sheets deform significantly (indicated by the label "Bent" in the figure). Significant deformations are seen to occur for E_v as small as 0.8–1, i.e., approximately ten times smaller than in the single-sheet case. Sheet proximity has thus a strong effect on the morphology. Our simple model provides a criterion for which the curvature becomes larger than the experimental resolution $\kappa_r = 0.02/L$. This criterion defines two regions in the morphology diagram delimited by the dashed line of equation $d/L = KE_v/[\kappa_r L(E_v^c - E_v)]$ in Fig. 5. The model predicts a much larger amplitude of deformation than observed in the experiments, but a similar trend with respect to E_v. Indeed, the value of K used in Fig. 5, $K = 0.02$, is smaller than the one obtained from fitting the lateral force profiles of Fig. 4(b), $K \simeq 0.4$. The overestimation of the amplitude of deformation in the model likely originates from two aspects of the quasistatic approximation we used: first, we neglected the hydrodynamic drag force in the normal direction to the sheets, which delays the curvature response time; second, we assumed that the compressive force f_t is constant while in the experiments the sheets tumbles and thus are not submitted to a constant force. But it can be seen accounting for the difference in the value of K that the model is in reasonably good agreements with experimental data for $d/L \gtrsim 0.05$, as the dashed line in this interval separates the circles from the squares symbols with the correct scaling law in L/d. For $d/L \lesssim 0.05$, the sheets are observed to remain straight during the tumbling motion for all E_v tested and the L/d prediction fails. The experimental data of Fig. 5 reveal thus that the relation between the separation distance and the critical elastoviscous number to observe significant bending is non monotonic. Further experimental and simulation results of $\bar{\kappa}_{\max}L$ versus d/L for fixed E_v are shown in the Supplemental Material to give further evidence that the relation is nonmonotonic [21]. Lubrication forces between two plates separated by a distance d scale as $1/d^3$ for a normal displacement [41] and so are dominant at small distances over the dipolar forces. The timescale for the growth of the deformation in the case of a steady compressive force and lubrication scales as $(L/d)^3\tau$ [41] where $\tau = \eta L^3/B$ is the elastoviscous timescale. This timescale is much longer than the tumbling timescale $1/\dot{\gamma}$ for moderate $E_v = \dot{\gamma}\tau$ and small d/L. Thus, lubrication forces constrain dynamically the deformation for very small distances and moderate E_v. The convex shape is not observed in every experimental case, because for large distance between the sheets ($d/L > 0.5$) the centers of mass of the sheets are convected by the flow and thus the sheets are not always perfectly "in registry." A plot showing the amplitude of the maximum curvature of the convex shape from simulations can be found in the Supplemental Material, where experimental videos of the pair of sheets in which the convex shape is observed are also provided [21].

VI. CONCLUSION

In this study we measured for the first time the effective buckling threshold, which we define as the threshold to observe significant bending, for a pair of flexible sheets suspended in a viscous simple shear flow as function of the sheet-sheet distance. In experiments, we obtain a value of the critical elastoviscous number for buckling of a single rectangular sheet of $E_v^c \simeq 11$. This number is quite close to the one we obtain form 2D simulations, $E_v^c \simeq 8$. Our main result is the demonstration of a large reduction, by about a factor of ten, of the elastoviscous number for which a close pair of parallel sheets bend significantly. This reduction is caused by the dipolar flow disturbance induced by one sheet. This disturbance induces a lateral force on the second sheet. With a minimal model we showed that this lateral force enhances the effect of the compressional force experienced by the pair when oriented along the compressional axis of the shear flow. Furthermore, we showed that the dipolar flow disturbance induces bending also when the pair is oriented in the extensional quadrant. Experiments and simulations suggest that the amplitude of bending is inversely proportional to the distance between the sheets. For small separations, the lubrication force prevails and limits the dynamical deformation of the sheets. The competition between the dipolar enhancement and lubrication leads to a nonmonotonic relation between distance and effective buckling threshold.

In the applied context of designing macroscopic materials, for instance nanocomposites, from sheetlike nanoparticles by liquid-based methods (as ink printing, coating, polymer nano-composite

processing and liquid-phase exfoliation [10,11]), our results suggest that at finite volume fraction hydrodynamic interactions could amplify deformations induced by the shear flow. The effect could alter thermal, optical or electrical properties that are dependent on the nanoparticle shape. In the context of rheology, by focusing on hydrodynamic pair-interactions our results provide a first step to understand the dynamics of flexible sheets in suspension. In particular, it has been evidenced for suspensions of fibers that buckling produces normal stress differences [28]. Hence, our results suggest that the microstructure of a suspension of sheetlike particles, including the statistics of pair-particle orientation and interparticle distance, could have a profound influence on the rheology by affecting the instantaneous particle shape. Therefore, the microstructure of suspensions of sheetlike particles should be well-characterized in future rheological studies.

ACKNOWLEDGMENTS

---

[1] B. W. Soh, A. R. Klotz, R. M. Robertson-Anderson, and P. S. Doyle, Long-lived self-entanglements in ring polymers, Phys. Rev. Lett. **123**, 048002 (2019).

[2] M. Abkarian, M. Faivre, and A. Viallat, Swinging of red blood cells under shear flow, Phys. Rev. Lett. **98**, 188302 (2007).

[3] K. S. Silmore, M. S. Strano, and J. W. Swan, Buckling, crumpling, and tumbling of semiflexible sheets in simple shear flow, Soft Matter **17**, 4707 (2021).

[4] S. W. Marlow and P. D. Olmsted, The effect of shear flow on the Helfrich interaction in lyotropic lamellar systems, Eur. Phys. J. E **8**, 485 (2002).

[5] E. Lauga, Bacterial hydrodynamics, Annu. Rev. Fluid Mech. **48**, 105 (2016).

[6] J. G. Oldroyd and A. H. Wilson, The elastic and viscous properties of emulsions and suspensions, Proc. R. Soc. London A **218**, 122 (1953).

[7] P. G. De Gennes, Coil-stretch transition of dilute flexible polymers under ultrahigh velocity gradients, J. Chem. Phys. **60**, 5030 (1974).

[8] V. Kantsler and R. E. Goldstein, Fluctuations, dynamics, and the stretch-coil transition of single actin filaments in extensional flows, Phys. Rev. Lett. **108**, 038103 (2012).

[9] R. Larson, The rheology of dilute solutions of flexible polymers: Progress and problems, J. Rheol. **49**, 1 (2005).

[10] V. Nicolosi, M. Chhowalla, M. G. Kanatzidis, M. S. Strano, and J. N. Coleman, Liquid exfoliation of layered materials, Science **340**, 1226419 (2013).

[11] S. Naficy, R. Jalili, S. H. Aboutalebi, R. A. Gorkin III, K. Konstantinov, P. C. Innis, G. M. Spinks, P. Poulin, and G. G. Wallace, Graphene oxide dispersions: tuning rheology to enable fabrication, Mater. Horiz. **1**, 326 (2014).

[12] K. R. Paton, E. Varrla, C. Backes, R. J. Smith, U. Khan, A. O'Neill, C. Boland, M. Lotya, O. M. Istrate, P. King, T. Higgins, S. Barwich, P. May, P. Puczkarski, I. Ahmed, M. Moebius, H. Pettersson, E. Long, J. Coelho, S. E. O'Brien *et al.*, Scalable production of large quantities of defect-free few-layer graphene by shear exfoliation in liquids, Nat. Mater. **13**, 624 (2014).

[13] Y. Yu and M. D. Graham, Coil–stretchlike transition of elastic sheets in extensional flows, Soft Matter **17**, 543 (2021).

[14] V. Labalette, A. Praga, F. Girard, M. Meireles, Y. Hallez, and J. F. Morris, Shear-induced glass-to-crystal transition in anisotropic claylike suspensions, Soft Matter **17**, 3174 (2021).

[15] Y. Xu and M. J. Green, Brownian dynamics simulations of nanosheet solutions under shear, J. Chem. Phys. **141**, 024905 (2014).

[16] Y. Yu and M. D. Graham, Wrinkling and multiplicity in the dynamics of deformable sheets in uniaxial extensional flow, Phys. Rev. Fluids **7**, 023601 (2022).

[17] G. Salussolia, C. Kamal, J. Stafford, N. Pugno, and L. Botto, Simulation of interacting elastic sheets in shear flow: Insights into buckling, sliding, and reassembly of graphene nanosheets in sheared liquids, Phys. Fluids **34**, 053311 (2022).

[18] K. S. Silmore, M. S. Strano, and J. W. Swan, Thermally fluctuating, semiflexible sheets in simple shear flow, Soft Matter **18**, 768 (2022).

[19] Y. Wang, S. Wang, P. Li, S. Rajendran, Z. Xu, S. Liu, F. Guo, Y. He, Z. Li, Z. Xu, and C. Gao, Conformational phase map of two-dimensional macromolecular graphene oxide in solution, Matter **3**, 230 (2020).

[20] B. Metzger, and J. E. Butler, Clouds of particles in a periodic shear flow, Phys. Fluids **24**, 021703 (2012).

[21] See Supplemental Material at http://link.aps.org/supplemental/10.1103/PhysRevFluids.8.124103 for the velocity field; the result of the linear interpolation on the angle variation corresponding to Fig. 3(a); the log-log version of Fig. 2(b); the maximum curvature vs E_v for a single sheet from simulations; the normalized curvature $\bar{\kappa}L$ vs normalized time $\dot{\gamma}t$ for a sheet pair separated by $d/L \simeq 0.09$ for $E_v \simeq 7.5$ in the experiment; the maximum normalized curvature for different normalized separation distances d/L and elastoviscous numbers E_v from simulations; the plot of the amplitude of the maximum curvature of the convex shape from simulations.

[22] D. J. Smith, A boundary element regularized stokeslet method applied to cilia-and flagella-driven flow, Proc. R. Soc. A **465**, 3605 (2009).

[23] S. D. Olson and L. J. Fauci, Hydrodynamic interactions of sheets vs filaments: Synchronization, attraction, and alignment, Phys. Fluids **27**, 121901 (2015).

[24] T. D. Montenegro-Johnson, L. Koens, and E. Lauga, Microscale flow dynamics of ribbons and sheets, Soft Matter **13**, 546 (2017).

[25] C. Pozrikidis *et al.*, *Boundary Integral and Singularity Methods for Linearized Viscous Flow* (Cambridge University Press, Cambridge, UK, 1992).

[26] R. Cortez, The method of regularized stokeslets, SIAM J. Sci. Comput. **23**, 1204 (2001).

[27] L. J. Fauci and C. S. Peskin, A computational model of aquatic animal locomotion, J. Comput. Phys. **77**, 85 (1988).

[28] L. E. Becker and M. J. Shelley, Instability of elastic filaments in shear flow yields first-normal-stress differences, Phys. Rev. Lett. **87**, 198301 (2001).

[29] J. Bico, E. Reyssat, and B. Roman, Elastocapillarity: When surface tension deforms elastic solids, Annu. Rev. Fluid Mech. **50**, 629 (2018).

[30] B. Audoly and Y. Pomeau, *Elasticity and Geometry* (Oxford University Press, Oxford, UK, 2000).

[31] O. du Roure, A. Lindner, E. N. Nazockdast, and M. J. Shelley, Dynamics of flexible fibers in viscous flows and fluids, Annu. Rev. Fluid Mech. **51**, 539 (2019).

[32] G. B. Jeffery and L. N. G. Filon, The motion of ellipsoidal particles immersed in a viscous fluid, Proc. R. Soc. London Ser. A **102**, 161 (1922).

[33] C. Kamal, S. Gravelle, and L. Botto, Effect of hydrodynamic slip on the rotational dynamics of a thin brownian platelet in shear flow, J. Fluid Mech. **919**, A1 (2021).

[34] P. S Lingard and R. L Whitmore, The deformation of disc-shaped particles by a shearing fluid with application to the red blood cell, J. Colloid Interface Sci. **49**, 119 (1974).

[35] S. Poincloux, T. Chen, B. Audoly, and P. M. Reis, Bending response of a book with internal friction, Phys. Rev. Lett. **126**, 218004 (2021).

[36] G. Wang, Z. Dai, J. Xiao, S. Feng, C. Weng, L. Liu, Z. Xu, R. Huang, and Z. Zhang, Bending of multilayer van der Waals materials, Phys. Rev. Lett. **123**, 116101 (2019).

[37] Four experimental data points are missing at $\dot{\gamma}t \simeq 0.17$ and $\dot{\gamma}t \simeq 5.4$ due to a camera software issue, which does not influence our observation of the concave and convex shape.

[38] E. Guazzelli and J. Morris, *A Physical Introduction to Suspension Dynamics* (Cambridge University Press, Cambridge, UK, 2012).

[39] G. K. Batchelor, The stress generated in a nondilute suspension of elongated particles by pure straining motion, J. Fluid Mech. **46**, 813 (1971).

[40] J. S. Wexler, P. H. Trinh, H. Berthet, N. Quennouz, O. du Roure, H. E. Huppert, A. Lindner, and H. A. Stone, Bending of elastic fibres in viscous flows: The influence of confinement, J. Fluid Mech. **720**, 517 (2013).

[41] N. Sridhar, D. J. Srolovitz, and B. N. Cox, Buckling and post-buckling kinetics of compressed thin films on viscous substrates, Acta Mater. **50**, 2547 (2002).